

Petrophysical Properties of IDDP-2 Core Samples from Depths of 3650 to 4650m

Benoit Gibert¹, Didier Loggia¹, Fleurice Parat¹, David Escobedo¹, Léa Levy^{2,3}, Gudmundur Omar Fridleifsson⁴,
Philippe A. Pezard¹, Nicolas Marino¹, Robert A. Zierenberg⁵

¹Laboratoire Géosciences Montpellier, Université de Montpellier, France ²Ecole Normale Supérieure, Paris, France, ³University of Iceland, ⁴IDDP office and HS Orka, Iceland, ⁵University of California, Davis, USA.

Keywords: IDDP-2, drilling, porosity, electrical conductivity, acoustic properties, supercritical geothermal reservoir

ABSTRACT

As part of the exploration of supercritical geothermal reservoirs at the Reykjanes Peninsula, SW Iceland, the IDDP consortium has accomplished a series of exploratory drillings and coring in order to investigate the physical conditions at depths of 4-5 km in high temperature-high pressure hydrothermal environments. A set of 21 cylindrical mini-cores samples extracted from IDDP-2 core between 3638m to 4654m depth were studied to identify their alteration mineralogy and petrophysical properties. Optical and SEM observations from thin sections indicate that samples are medium to fine grained diabase intrusions showing granular holocrystalline textures. Mineral compositions from XRD on powders and from SEM observations on thin sections indicate that the rocks are composed of plagioclase and amphibole (80-90%), replacing primary augite phenocrysts, along with magnetite and ilmenite and minor amounts of quartz. Enstatite and biotite are present in the deepest cores, below 4500m. Petrophysical properties such as porosity, acoustic velocities (V_p-V_s) and electrical conductivity were first measured on one inch diameter mini-core samples at room conditions in dry and saturated conditions. Porosity is generally low, ranging from 0.4 to 2.9 %. Electrical conductivity, measured at 10³ Hz as a function of pore fluid conductivity, indicates an unusual and low electrical tortuosity and cementation index for dolerites (2.3-10.0 and 1.2-1.6, respectively). P-wave velocity is higher by 30 % on average when the sample is saturated with water, compared to dry conditions. Both acoustic and electrical properties indicate that interconnected microcracks and fissures dominate porosity. Electrical conductivity measurements at 100 MPa of confining pressure – i.e. relevant for *in-situ* conditions and up to 600°C, under both dry and fluid-saturated conditions, indicate that the total conductivity of the sample increases by more than one decade from dry to fluid-saturated conditions. Acoustic properties measurements at room temperature and up to 300 MPa of confining pressure, indicate that P- and S-wave velocities increase in a non-linear and reversible manner when pressure increases. This behaviour is attributed to microcrack closure with increasing pressure. Crack density calculation shows that relative high crack density (>0.3) is preserved at effective pressure corresponding to in-situ conditions. Our results indicate that the density of microcracks controls the physical properties of rock samples over the whole investigated section. Microcracks may result from recent hydrothermal circulations, as suggested by Violay et al. (2010) on samples from samples collected in the sheeted dike complex cored by IODP hole 1256D. Microcracks may also arise from drilling operations, where intense in-situ cooling and later decompression generates mechanical stresses linked to mineral contraction. Finally, the comparison of high-pressure core measurements to data from down hole geophysical tools, large scale MT, and seismic investigations in the Reykjanes peninsula is compatible with the presence of supercritical fluids at depth.

1. INTRODUCTION

IDDP-2 borehole was drilled in 2017 at the Reykjanes peninsula in SW-Iceland in order to explore the feasibility of supercritical geothermal reservoirs exploitation. Spot cores recovered deeper than 3500 m provide a unique opportunity to investigate alteration processes under high-temperature hydrothermal conditions, as well as to evaluate the petrophysical properties of supercritical reservoirs. Among these properties, porosity and permeability are key physical properties, largely controlling the localization, intensity and duration of hydrothermal circulation. For instance, numerical simulations of fluid flow around a magmatic body have shown that a supercritical aureole can be preserved around a high temperature intrusion for a given range of in-situ permeability (Scott et al., 2016). In intrusive crystalline rocks, porosity and permeability are primarily controlled by microcrack geometry and distribution. Microcracks may result from different processes, such as dissolution/precipitation and mass transport due to fluid/rock interactions, microfracturing and dilatance due to tectonic activity and related rock deformation in the brittle field (e.g. Fortin et al., 2011, Violay et al., 2015). Thermally induced cracks can be generated by local temperature variations, caused by either magmatic intrusions or hydrothermal fluids circulation (e.g., Boudier et al., 2005, Fortin et al., 2011). At the well scale, cracks can be produced by intense cooling and decompression of rocks, in particular in deep and hot environments where thermal damage may significantly increase the permeability (e.g. Gasshemi and Tarasovs, 2015, Peter-Borie et al., 2018, Peter-Borie et al. 2019). Evaluating the origin of the in-situ microfracturation state of rocks under these extreme conditions is therefore a key issue for the characterization of the reservoir in terms of porosity, permeability and exploration of the related geothermal resources. Linking macroscopic physical properties, that can be surveyed by geophysical soundings, to microscopic parameters related to fracturing is of key interest. For instance, investigations of the root of the sheeted dikes complex sampled by IODP hole 1256D have been conducted to establish relationships between alteration processes, porosity, electrical and acoustic properties of rocks at the borehole scale (Violay et al., 2010). Linking acoustic properties to microfracturing in Icelandic basalts has contributed to efforts to invert large-scale tomographic data in terms of microscopic parameters, such as crack density, pore geometry and fluid parameter (Adelinet et al., 2011). These parameters can finally be connected to permeability, which is an important property when considering reservoir evaluation (e.g. Gueguen and Dienes, 1989).

In this work, we present a petrophysical characterization of the 13 IDDP-2 cores sampled between 3560 and 4650m depth. Porosity, electrical conductivity and acoustic properties have been investigated at room conditions, but also at temperature and pressure corresponding to in-situ conditions in order to connect microscopic observations to borehole measurements and large-scale geophysical surveys.

2. BACKGROUND: ELECTRICAL AND ACOUSTIC PROPERTIES

Seismic and electromagnetic soundings are commonly used in geothermal exploration. These methods are sensitive to in-situ temperature, pressure, nature of fluids and alteration minerals, and depend upon the acoustic velocities and electrical conductivity of the rocks, respectively. We present in the following a summary of acoustic and electrical properties of rocks in general.

2.1 Electrical conductivity

The total electrical conductivity of rocks is considered to be the sum of three contributions in parallel: electrolyte (water with ions) in the porous media, the rock/water interface known as surface conduction (e.g. Waxman and Smits, 1968) and intra-mineral conduction (Pezard et al., 1991, Einaudi et al., 2005, Nono et al., 2018, Lévy et al., 2018) (eq.1).

$$\sigma_r(T, P) = \frac{\sigma_f(T, P)}{F(T, P)} + \sigma_s(T, P) + \sigma_{\text{minerals}}(T, P) \quad (1)$$

where σ_f , σ_s and σ_{minerals} are the electrolytic, surface and intra-mineral conductivity, respectively. σ_r is the total electrical conductivity of the saturated rock sample and F is the formation factor. F is used to describe the topology of the porous medium; it is related to porosity by the “so called” cementation index, m , where:

$$F = \Phi^{-m} \quad (2)$$

m indicates the degree of interconnection between pores in 3D but also describes the non-uniformity of conductive channels. m close to unity indicates that porosity is dominantly related to fractures, while $m > 2$ indicates that porosity is of granular and interconnected type. In low porosity rocks, the electrical tortuosity can be defined as (Pezard, 1990):

$$\tau = F \cdot \phi \quad (3)$$

It provides an indication of the geometrical complexity of the electrical current path.

The temperature and pressure influence on equation 1 parameters are important to simulate IDDP-2 in-situ conditions. They are generally poorly constrained, due to the limited number of experimental electrical conductivity studies at high pressure and temperature conditions (Glover et al., 1992, Kummerow and Raab, 2015, Nono et al., 2018). However, it has been shown that fluid salinity and nature (liquid or supercritical) have a strong influence on electrical conductivity, with large changes in fluid conductivity, but also in surface conduction (Synmio et Keppler, 2017, Nono et al., 2018). Given the very high temperatures reached in the IDDP-2 hole, intra-mineral conduction (ionic and electronic) may also contribute significantly to the electrical transport, in particular in Fe-bearing minerals and phyllosilicates (Pezard et al., 1991, Einaudi et al., 2005, Nono et al., 2018, Lévy et al., 2018). Therefore, it is important to take these minerals into consideration when analysing electromagnetic soundings.

2.2 Acoustic properties

Seismic velocities depend on elastic properties of the solid matrix, porosity, pore topology and pore fluid nature. Thus, they can be interpreted in terms of microscopic parameters (e.g., Adelinet et al., 2011). In particular, microcracks play a major role on acoustic wave propagation in crystalline rocks. For a given sample, one can define an effective medium with spherical pores and randomly oriented microcracks embedded in a solid matrix. Crack density is defined as $\rho_c = \frac{1}{V} \sum^N c_i^3$ where N is total number of cracks in a given representative elementary volume V and c_i is the radius of the i th crack. The crack aspect ratio is defined as the mean ratio between the aperture and the diameter of the cracks. As microcracks are very compliant, their presence has a strong impact on both absolute values and pressure dependence of acoustic velocities. Laboratory measurements of acoustic velocities can be interpreted in terms of crack density by the mean of the elastic wave propagation theory. The theoretical model of Fortin et al. (2007), where the porosity is made of spheroidal pores of porosity ϕ_p and penny-shaped cracks with a very low porosity ϕ_c is used in the following. In this model, the crack density can be calculated from the porosity, the bulk and shear modulus of the solid matrix and the bulk and shear modulus of the rock. The matrix moduli can be calculated from the elastic moduli of the different minerals present into the rock, by a weighted average with respect to their respective proportions. The moduli of the rock are calculated from the P- and S-wave velocities measured at high frequency (MHz) and dry conditions (i.e. unsaturated) in the laboratory. The crack density of the dry rock can be obtained, for instance, using the equations 8 and 9 in Fortin et al. (2007).

Extrapolation of laboratory measurements (at a high frequency of 1 MHz, HF, and dry conditions) to in-situ conditions (Low Frequency, LF, seismic waves and saturated conditions) can be done using the Biot-Gassmann theory (Gassmann, 1951). In this theory, the LF saturated shear modulus equals the HF dry shear modulus, while the LF saturated bulk modulus depend on the HF dry rock bulk modulus, the porosity, the solid matrix moduli, and the fluid compressibility (e.g., Adelinet et al., 2011, equation 11). LF P- and S- waves velocities are then determined from the saturated moduli. This model assumes a homogeneous, isotropic poroelastic media in undrained conditions, but no assumptions are made on the nature and geometry of the pores.

3. SAMPLES

A set of 21 cm-scale cylindrical mini-cores extracted from the 13 spot cores drilled from 3648m to 4654m were studied in order to identify their mineralogy and physical properties (Figure 1). Most rocks within this interval are composed of fine- to medium-grained diabase dikes and basaltic intrusions, as described in Fridleifsson et al. (2018), and are interpreted as samples from a sheeted dike complex.

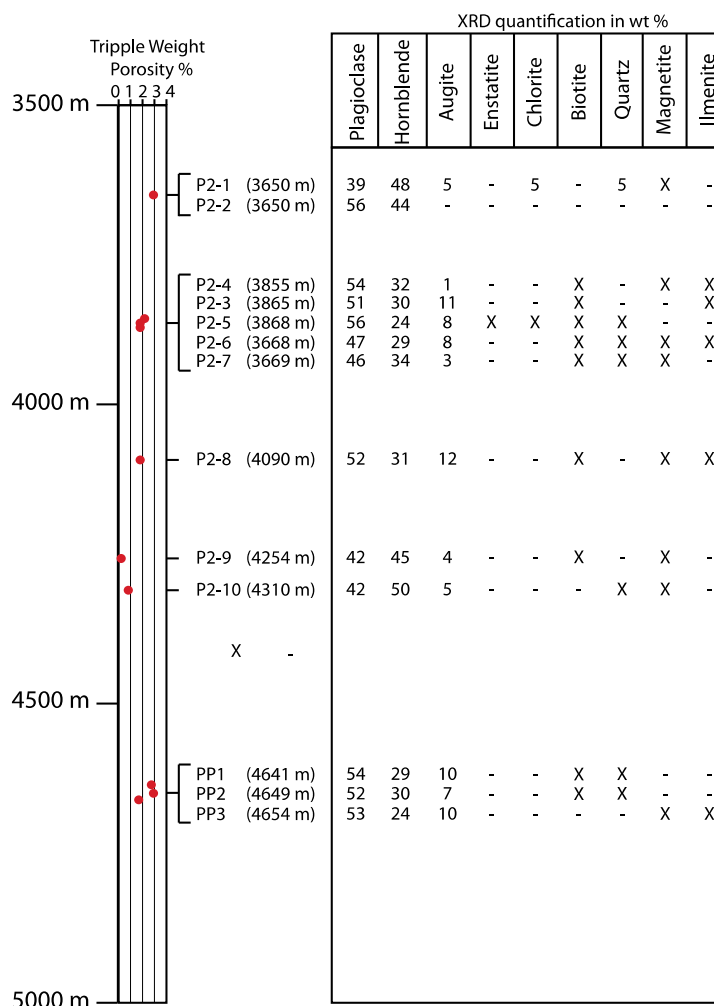


Figure 1: Depth, porosity and mineralogy from XRD Rietveld analysis of the 13 IDDP-2 samples.

Optical and SEM observations on thin sections indicate that samples are medium to fine grained diabase intrusions with granular holocrystalline textures. The mineral assemblages from XRD analyses indicate that the rocks are mostly composed of plagioclase and hornblende (80 to 90 vol.%). Hornblende is a secondary mineral from alteration of primary augite phenocrysts. Unaltered augite phenocrysts are almost absent in shallow samples (<2%), but secondary hydrothermal clinopyroxenes becomes more abundant in the deepest section. Accessory minerals are magnetite, ilmenite, and secondary quartz, biotite and orthopyroxene.

Samples **P2-1** and **P2-2** (3648m depth) are fined grained diabase dikes (Figure 2a) presenting porphyritic-aphanitic texture. The mineralogy is dominated by acicular plagioclase and uralitic textures in which amphibole pseudomorphs replace augite. Sample P2-1 presents a fracture filled with plagioclase, and chlorite minerals.

Samples **P2-3**, **P2-4**, **P2-5**, **P2-6**, **P2-7** and **P2-8** (3855 to 3865m depth) consist of medium grained altered diabase dike showing porphyritic texture. The mineralogical composition is dominated by euhedral plagioclase and hornblende. Augite, magnetite and ilmenite are also present (Fig. 2b). Chlorite is absent from the sample P2-5 to the deepest part of the well.

Sample **P2-9** (4254m depth) is a fined grain diabase altered to amphibole presenting microlites of plagioclase and clinopyroxene and fine veins filled with hornblende (Figure 2c). Sample **P2-10** (4310m depth) is a medium to fined grained diabase of porphyritic-aphanitic texture where phenocrysts were plagioclase and clinopyroxenes now replaced by hornblende. Other accessory minerals are augite, magnetite and quartz.

Samples **PP1** and **PP2** (4641 to 4649m depth) show a primary assemblage of plagioclase, augite and titanomagnetite. Accessory minerals are quartz, enstatite, biotite, magnetite and ilmenite (Figure 2d). Sample **PP3** (4654m depth) is a doleritic dike presenting plagioclase, hornblende, augite, enstatite and quartz, magnetite and ilmenite as accessory minerals.

All the samples exhibit open, non-mineralized microcracks that cross cut minerals and grain boundaries (figure 2 and 3). This fracturing is more intense in the deepest samples, in particular in samples PP1 and PP2.

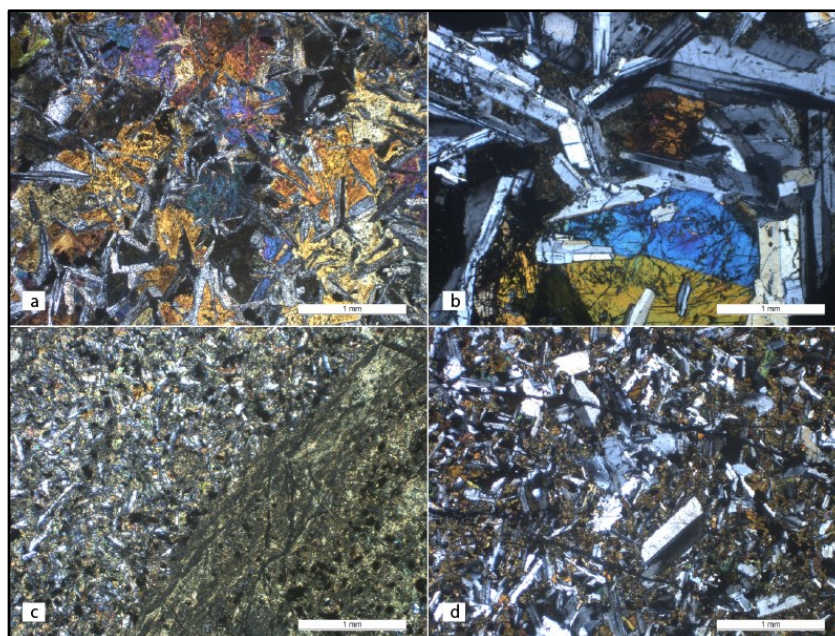


Figure 2: Microphotographs of thin sections in cross-polarized light. a) Sample P2-2; b) Sample P2-4; c) Sample P2-9; d) Sample PP2.

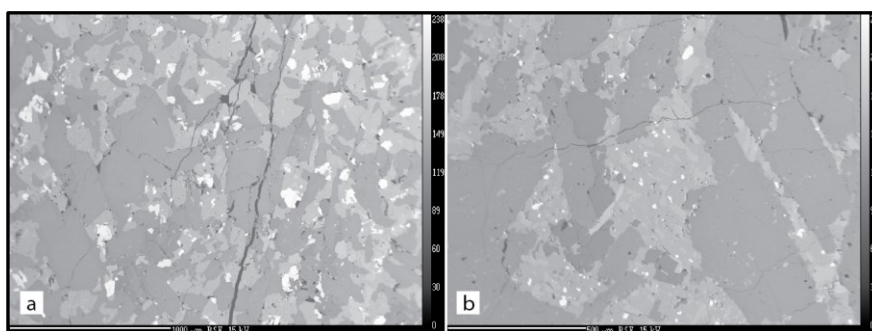


Figure 3: BSE images for samples: a) PP2 and b) PP3

4. PETROPHYSICAL METHODS.

A set of 21 mini-cores of 25.4mm in diameter and from 10 to 50 mm in length were drilled in the direction perpendicular to the core axial direction. The suffix *a-b-c* indicate that several mini-cores have been drilled from one single core (Table 1). Given the low amount of available material, only three 10 cm long cores, extracted from the deepest part of the well (PP1, PP2, PP3), allowed drilling several mini-cores that have been used for destructive experiments at high temperature/high pressure conditions. The samples were first dried at least 48h at 60°C and the dry mass was measured. Then they were placed in a vacuum chamber and saturated with degassed water. Under saturated conditions, porosity and grain density were determined by the triple weight method, where sample mass was measured under dry, saturated and immersed conditions. The estimated uncertainty on porosity is on average 5-10%.

Electrical properties were first determined at room conditions for saturated samples. Each core was saturated with electrolytes of different salinities, using aqueous NaCl solutions at variable concentrations and conductivity (from 0.02 S.m⁻¹ to 5.36 S.m⁻¹). Electrical conductivity is determined from the impedance measured at a frequency of 1 kHz with a Solarton 1260 impedance-meter using a two-pole configuration. After changing the salinity of the pore fluid, all the samples were kept together in the same fluid for at least one month in order to achieve rock/fluid equilibrium and their conductivity was measured. Electrical parameters such as formation factor, surface conductivity, cementation index and tortuosity were determined from the relation between the bulk rock conductivity and the saturating fluid conductivity (equation 1, 2 and 3). The estimated uncertainty on electrical conductivity measurement is estimated to 2%.

At high pressure and temperature, the electrical conductivity was measured for only one sample (PP2) under dry conditions following the method used in Nono et al. (2018). Under saturated conditions, a modified set-up was used, and the impedance was measured using a radial configuration that allowed better stability and reproducibility at high temperature.

Acoustic properties (P- and S-waves velocities) were measured using ultrasonic transducers at a frequency of 500 kHz using the time of flight method. At room conditions, the velocities were measured in dry and saturated conditions on all the samples. For two samples (PP2 and PP3), the velocities were determined at high pressure up to 300 MPa in a Paterson gas pressure apparatus under dry conditions only. Uncertainty on measured velocities is of 1% on average.

5. RESULTS

5.1 Porosity and electrical properties.

The experimental results are summarized in table 1.

Table 1: Triple Weight Porosity, matrix grain density and electrical properties of IDDP-2 samples.

Sample	Depth	TW porosity (%)	Matrix grain density ($\text{g}\cdot\text{cm}^{-3}$)	Formation factor	Surface conductivity ($\text{mS}\cdot\text{m}^{-1}$)	Cementation index	Tortuosity
P2-1	3648.03	2.9	3.01	322	0.39	1.63	9.4
P2-2a	3648.45	2.7	3.04	330	0.74	1.61	9.0
P2-2b	3648.45	2.7	3.04	235	0.35	1.51	6.4
P2-3	3865.58	2.2	3.00	207	0.49	1.40	4.6
P2-4	3855.72	1.8	3.00	218	0.38	1.34	4.0
P2-5a	3868.53	1.7	3.02	159	0.55	1.25	2.8
P2-5b	3868.53	1.8	3.02	195	0.43	1.31	3.5
P2-6a	3868.6	2.0	3.01	188	0.56	1.34	3.7
P2-6b	3868.6	2.0	3.02	201	0.85	1.35	4.0
P2-7a	3869.91	2.0	3.01	223	0.38	1.39	4.5
P2-7b	3869.91	2.2	3.01	184	0.58	1.36	4.0
P2-8	4090.03	1.8	3.03	182	0.78	1.29	3.2
P2-9	4254.68	0.3	3.04	640	0.15	1.11	1.9
P2-10	4310.06	0.9	3.01	270	0.44	1.19	2.4
PP1a	4641.41 to 4641.52	2.7	3.03	-	-	-	-
PP1b	4641.41 to 4641.52	2.5	3.03	64	0.15	1.13	1.6
PP2a	4649.25 to 4649.35	2.8	3.05	94	0.62	1.27	2.6
PP2b	4649.25 to 4649.35	2.9	3.05	92	0.30	1.27	2.6
PP3a	4654.20 to 4654.30	1.7	3.05	123	0.31	1.18	2.1
PP3b	4654.20 to 4654.30	1.5	3.05	162	0.52	1.22	2.5
PP3c	4654.20 to 4654.30	1.5	3.04	161	0.44	1.21	2.4

The porosity measured by the triple weight method varies from 0.3% to 2.9% (Table 1). Samples P2-9 and P2-10 have the lowest porosities (0.3% and 0.9%, respectively) whereas the other samples have a porosity between 1.8 and 2.9%. P2-9 and P2-10 have a very fine-grained texture, but also the highest alteration content (amphibole). The matrix grain density derived from porosity measurements varies by $\pm 0.04 \text{ g}\cdot\text{cm}^{-3}$ from a $3.03 \text{ g}\cdot\text{cm}^{-3}$ average.

Electrical conductivity as a function of saturating fluid conductivity is presented here (Figure 3) for a few representative samples with a log-log crossplot. The linear part indicates the range of fluid conductivity where pore fluid dominates the electrical conduction of the rock. At low fluid conductivity, a flattening of the curve is observed and is interpreted as an increasing contribution of surface conduction. Formation factor and surface conductivity were extracted from these experiments, using a linear fit (e.g. Lévy et al., 2018). Cementation index and tortuosity were calculated from equations 2 and 3 and triple weight porosity (Table 1).

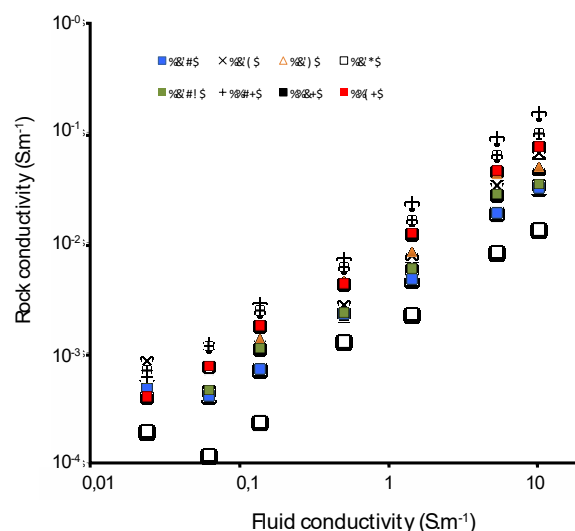


Figure 3: Bulk rock conductivity as a function of saturating fluid conductivity.

The formation factor appears poorly correlated to porosity (Figure 4), as observed on a set of doleritic rocks from the sheeted dike complex located in the hole 1256D (Violay et al., 2010). Deep samples from PP1 and PP2 cores have the lowest formation factor whereas shallower samples (P2-1 and P2-2) have the highest formation factor, but similar porosity as PP1 and PP2. Tortuosity and cementation index generally increase with porosity, hence samples PP1 and PP2 have the lowest values. These two samples probably have an important fracture dominated pore space compared to the other samples, explaining their lower tortuosity and m values (Figure 4). Formation factor, cementation index and tortuosity are much lower than in the non-granoblastic dikes and gabbro

from hole 1256D (Violay et al. 2010), indicating in IDDP-2 samples a better connexion of the pore space in presence of a major fracture dominated pore space. The surface conductivity is very low and not well correlated to porosity (Figure 4). Considering high fluid salinity in Reykjanes geothermal reservoir (sea water salinity), this contribution is weak and might be neglected with respect to the electrolytic conduction.

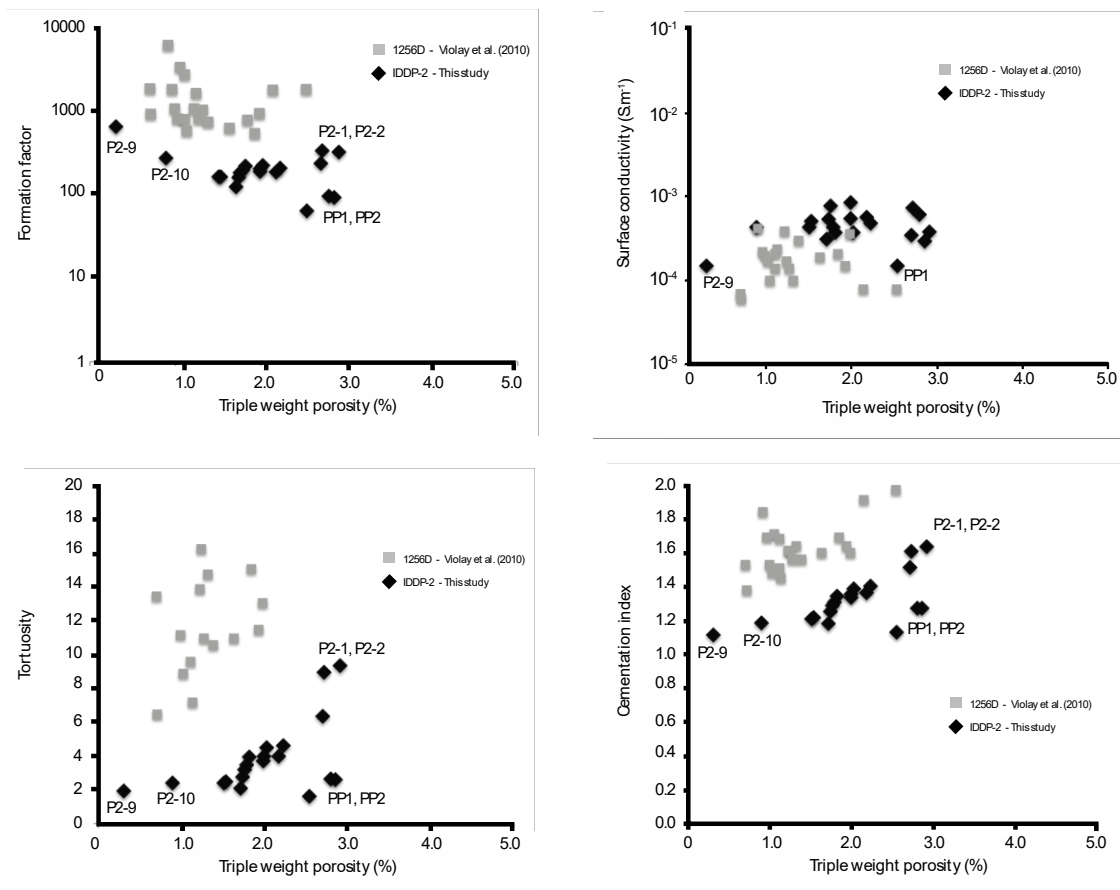


Figure 4: Electrical properties of IDDP-2 samples at room conditions as a function of triple weight porosity. For comparison, grey dots represent data on doleritic sheeted dikes and gabbros from IODP 1256D hole (Violay et al., 2010).

The electrical conductivity was measured for sample PP2 at constant confining pressure of 120 MPa, with a pore pressure of 35 MPa and up to 450°C corresponding to in-situ, supercritical conditions (Fridleifsson et al., 2018). The sample was saturated with a fluid with sea-water salinity (3.5wt% NaCl – 5.0 S.m⁻¹ at 25°C) close to that expected in the Reykjanes geothermal field. Confining pressure was first increased to 200 MPa at a constant pore pressure of 2 MPa (Figure 5A). Then confining pressure was decreased to 120 MPa and the pore pressure was increased to 35 MPa before increasing temperature (Figure 5B).

The electrical conductivity decreases non-linearly with pressure, where variation with pressure is higher in the low-pressure range (Figure 5A). It increases linearly with temperature up to 150°C and then stabilizes and reaches a maximum between 200 and 300°C, before decreasing when the temperature is raised up to 400°C (Figure 5B). The effect of temperature is very similar to that observed on dolerites by Nono et al. (2018) and Kummerow et al. (2018). It reflects the change in fluid properties with temperature. Beyond the critical point (406°C for a sea-water composition), the conductivity increases again, probably because of an increase of fluid-rock interactions enhanced by the fluid reactivity under these conditions (Kummerow et al., 2018).

The electrical conductivity of a dry mini-core from the PP2 sample was measured from 200°C to 700°C at a confining pressure of 120 MPa (Figure 5C, red dots). The dry conductivity displays a linear increase with reciprocal temperature, in agreement with a thermally activated mechanism. As discussed in Nono et al. (2018), electronic transport in Fe-bearing minerals, in particular amphibole, is probably the dominant transport mechanism. The present measurements are consistent with those of other dolerites from Reykjanes (well RN-19 and RN-30, Nono et al., 2018).

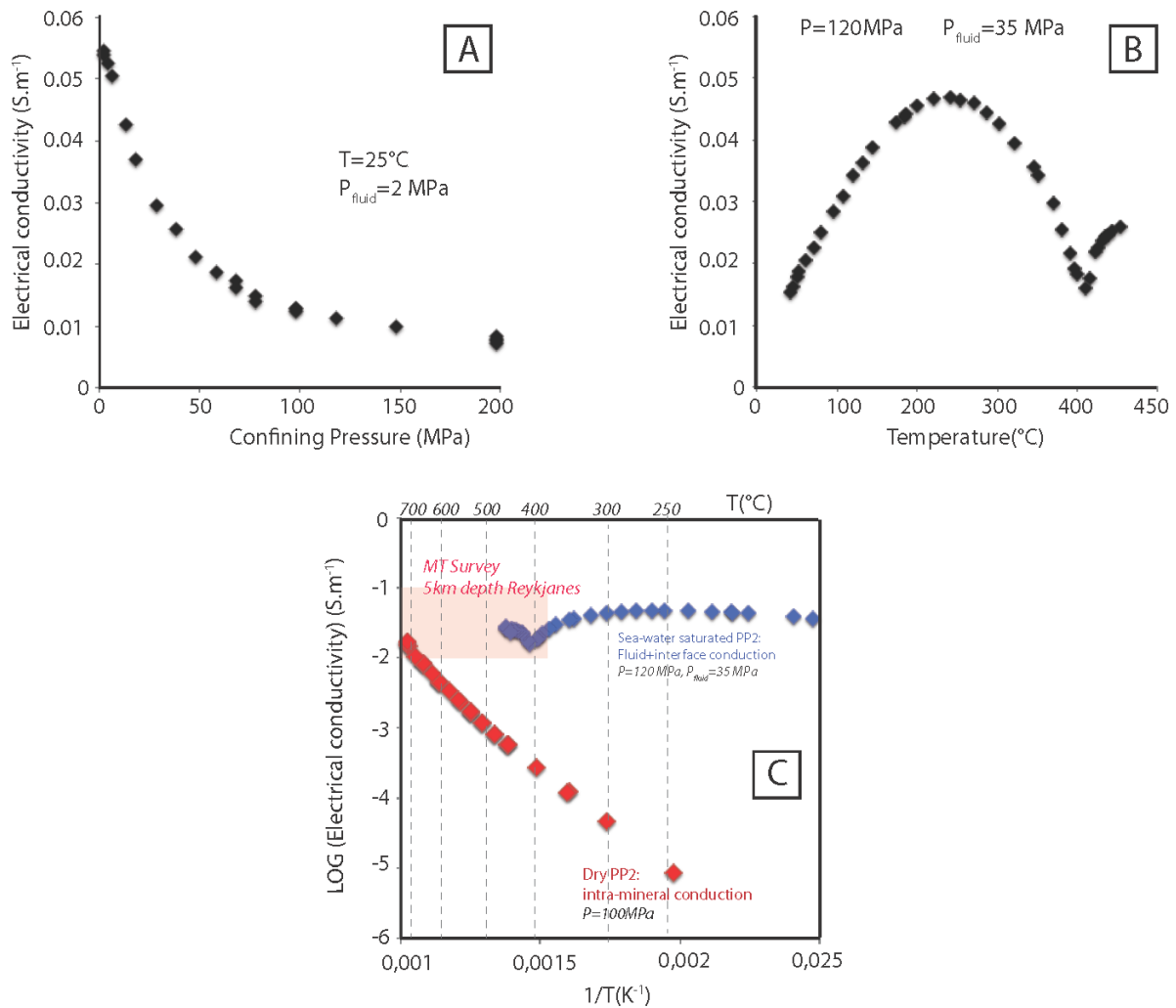


Figure 5: Electrical properties of the PP2 sample at high pressure and temperature. (A) Effect of confining pressure at T=25°C, with a pore fluid pressure of 2 MPa and a pore fluid conductivity of 5.0 S.m⁻¹. (B) Effect of temperature at a confining pressure of 120 MPa and a pore fluid pressure of 35 MPa. (C) Electrical conductivity under dry conditions (red dots) and saturated conditions (blue dots corresponding to graph B) – note the vertical log scale. Red rectangle is for electrical conductivity values determined from MT investigations at a depth of 5km at the tip of the Reykjanes peninsula where IDDP-2 well was drilled (Karlsdottir et al., 2018).

5.2 Acoustic properties.

Acoustic velocities measured in dry conditions display a high dispersion with porosity (Table 2, Figure 6). P2-9, P2-1 and P2-2 have the highest velocities, while PP1 and PP2 have the lowest ones, again possibly due to high fracture density. P-wave velocities (V_p) measured on saturated samples are much higher than the one measured in dry conditions. In contrast, S-waves velocities (V_s) are less affected by the effect of saturation. In dry conditions, the measured velocities are systematically lower than the ones measured by Violay et al. (2010), while they are very similar in saturated conditions.

Acoustic velocities were measured in dry conditions up to 300 MPa and at ambient temperature (25°C) on a PP2 sample. Both V_p and V_s increase non-linearly as a function of pressure (figure 7A). The rate of increase is high at low pressure and decreases up to the maximum pressure. The V_p/V_s ratio increases rapidly with pressure, up to 50 MPa, and remains nearly constant with an average of 1.73 ± 0.15 up to 300 MPa (Figure 7B).

In order to quantify the effect of microcracks on acoustic velocities, the rock matrix moduli are calculated from mineral elastic moduli and mineral content, considering a Voigt-Reuss-Hill averaging scheme. For simplicity, only plagioclase, amphibole and augite were considered in the calculations. Elastic moduli of these minerals were extracted from Brown et al. (2016), Brown et Abramson (2016) and Weidner et Vaughan (1982), respectively. The elastic moduli averaged over all the IDDP-2 samples are $K_0 = 87.4 \pm 3.5$ GPa and $G_0 = 50.5 \pm 3.7$ GPa. The resulting values of compressional and shear waves velocities of the matrix, respectively $V_p^0 = \sqrt{\frac{K_0 + 4/3 G_0}{\rho_{dry}}} = 7180 \pm 192$ m.s⁻¹ and $V_s^0 = \sqrt{\frac{G_0}{\rho_{dry}}} = 4100 \pm 150$ m.s⁻¹, are supposed to be equal to the ones measured at very high confining pressure, where porosity vanishes (grey lines in figure 7A). These predicted velocities are significantly higher than the experimental ones measured at the maximum pressure ($V_p^{dry} = 6340$ m.s⁻¹ and $V_s^{dry} = 3580$ m.s⁻¹), indicating a preservation of microcracks at this confining pressure.

Table 2: P- and S-wave velocities of IDDP-2 samples in dry and saturated conditions.

Sample	Vp dry (m.s ⁻¹)	Vp sat. (m.s ⁻¹)	Vs dry (m.s ⁻¹)	Vs sat. (m.s ⁻¹)
P2-1	4654	5949	2734	3197
P2-2a	5111	6156	3203	3337
P2-2b	5068	6286	3066	3425
P2-3	4758	5961	2778	3419
P2-4	4372	6036	2747	3035
P2-5a	4272	5754	2489	2960
P2-5b	3982	5856	2506	3104
P2-6a	4095	5684	2519	2939
P2-6b	4196	5780	2580	2955
P2-7a	4422	5743	2622	2965
P2-7b	4553	5804	2759	3229
P2-8	-	5245	-	2577
P2-9	5921	6690	3541	3592
P2-10	4569	5965	2841	3102
PP1a	2360	4617	1486	2146
PP1b	2546	-	1509	-
PP2a	2339	4690	1510	-
PP2b	2315	4944	1319	2566
PP3a	4240	5505	2569	3046
PP3b	4303	5539	2611	2888
PP3c	4646	5652	2838	-

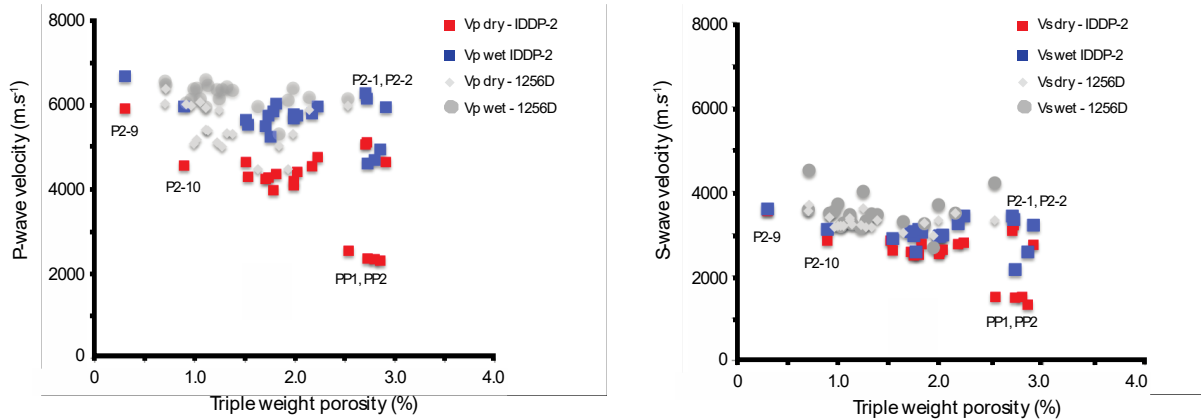


Figure 6: P-wave and S-wave velocities in dry (red dots) and saturated (blue dots) conditions as a function of triple weight porosity. Grey symbols represent measurements from doleritic sheeted dikes and gabbros cored in IODP 1256D hole (Violay et al., 2010).

From the matrix moduli and the elastic moduli of the rock sample extracted from direct P- and S- wave velocities measured on the dry sample, the evolution of crack density with pressure is determined, following Fortin et al. (2007) (Figure 7C). Crack density strongly decreases with pressure, indicating the closure of microcracks with increasing confining pressure. At the maximum confining pressure of 300 MPa, the crack density is the smallest, but cracks remain present with a crack density of nearly 0.12 (figure C).

From the measurements in dry conditions, the low frequency, seismic velocities of the water-saturated rock were calculated based on the Biot-Gassman theory (e.g. Adelinet et al., 2011) (figure 7A). First, the calculation has been performed considering a pure liquid water close to supercritical conditions, with a pore fluid pressure of 35 MPa and a temperature of 300°C. In such conditions, the density and bulk modulus of the fluid are 0.76 and 0.92 GPa, respectively (Wagner and Pruß, 2002). The resulting Vp plotted versus the effective pressure (defined here as the difference between the confining pressure and the pore pressure) shows that at low pressure, the fluid causes a strong increase of Vp, while at high pressure, Vp is nearly equal to the dry velocity. The presence of a fluid does not change the S-waves velocities since the shear modulus is assumed to be equal in dry and saturated conditions for a given effective pressure. A similar calculation has been done with pure water in the supercritical state, where pore pressure is of 35 MPa and T=450°C. Given the low elastic modulus (0.1GPa) of the considered fluid, both Vp and Vs curves are superimposed to the dry measurement curves, and then not represented in the figure 7A.

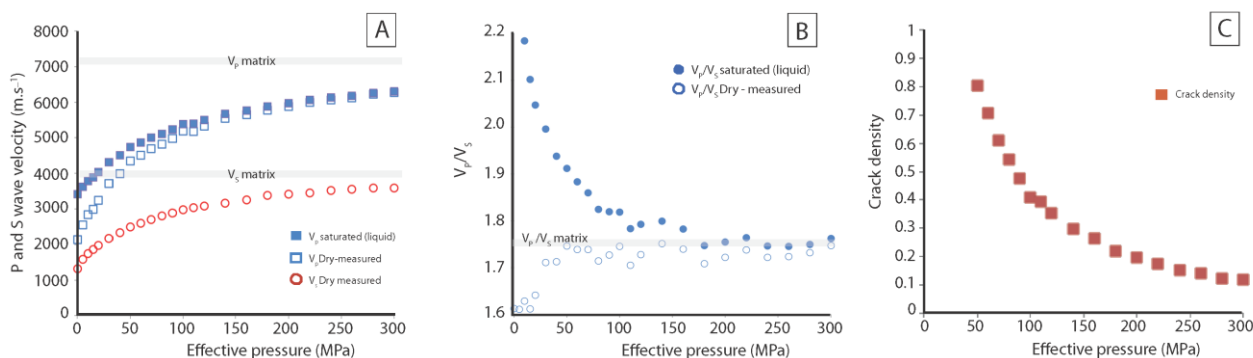


Figure 7: Acoustic properties of the PP2 samples. A) effect of effective pressure, taken as the difference between confining pressure and pore pressure, on velocities. In the case of dry conditions, the effective pressure equals the confining pressure. In the case of saturated conditions, pore pressure is taken at 35 MPa and P-wave velocity is calculated from dry measurement (see text for details). B) V_p/V_s ratio as a function of effective pressure calculated from A). C) Crack density calculated from dry V_p and V_s measurements.

6. DISCUSSION

Electrical and acoustic properties show that the samples are affected by a high degree of fracturing. Low cementation index and tortuosity indicate a highly connected porosity among the fractures. In comparison, samples from sheeted dike complex from fossil hydrothermally altered crust display a more complex pore space (Violay et al., 2010). The samples from the deepest part of the well (PP1 and PP2) are more affected by this fracturing in comparison to the shallowest ones P2-1 and P2-2. Samples displaying the lowest grain size and higher alteration content display the lowest porosity (P2-9, P2-10) but also the lowest cementation index and tortuosity. These observations, combined with macroscopic and microscopic observations indicate the presence of open, fresh and non-mineralized fractures that have been probably generated by high cooling rates, thermal damage and decompression during drilling operations (e.g. Peter-Borie et al., 2019). In addition, it was observed that coring in the three deepest cores was exceptionally smooth compared to coring in the shallowest samples. Although increasing temperature generally decreases the mechanical strength of the rocks in the brittle field (e.g. Violay et al. 2015), the effect of temperature alone cannot explain such a difference in mechanical strength. In-situ fracturing of rocks, prior to coring process, may explain the low mechanical strength of the deepest rocks, given that thermal and mechanical damage considerably affect the mechanical properties of rocks (e.g. Keshavarz et al., 2010). Although petrophysical properties at room conditions are probably not representative of in-situ conditions, they indicate that the modification of stress field and thermal cooling may drastically modify the porosity and transport properties in the vicinity of the well.

Pressurization of one sample up to in-situ pressure conditions (about 100-120 MPa of confining pressure) show a high pressure dependence of acoustic and electrical properties, which can be interpreted by the closure of microcracks (e.g. Fortin et al., 2011). At the highest pressure, acoustic properties indicate that crack density is relatively high (0.2 at 200 MPa) and that formation factor, although elevated ($F = \frac{\sigma_{rock}}{\sigma_{fluid}} \approx 500$ at 200 MPa) is compatible with crack preservation. Under these conditions, petrophysical parameters such as formation factor and acoustic velocities are similar to the ones measured in the sheeted dike complex and gabbro (e.g., Violay et al., 2010, Ildefonse et al., 2001).

Electrical conductivity measured close to in-situ conditions (120 MPa, $T > 400^\circ\text{C}$) indicates that the presence of fluid causes an increase by about two orders of magnitude of the conductivity, compared to dry conditions at 400°C . In-situ electrical conductivity, deduced from MT surveys in the same area at 4-5km depth (Karlsdottir et al., 2018) ranges between 0.01 and 0.05 $\text{S}\cdot\text{m}^{-1}$ (figure 5C). Electrical conductivity in dry conditions, where intra-mineral conduction dominates, can only explain these observations if in-situ temperature is higher than 700°C (Figure 5C). Thus, in the range of temperatures suggested by in-hole observations ($T = 400\text{--}500^\circ\text{C}$ at the bottom of the well, Fridleifsson et al., 2018), large-scale electrical anomalies can only be related to the presence of fluids. Mineral geochemistry (Zierenberg et al., 2020) and fluid inclusion data (Bali et al., 2020) suggest that in situ temperatures are close to 600°C . However, above the critical point, laboratory measurements are more uncertain, due to fluid-rocks interactions (e.g. Kummerow et al., 2018) that may modify the fluid composition and its electrical conductivity. Pore fluid pressure also influences the results as fluid conductivity significantly varies with pressure close to the critical point (e.g. Symio and Keppler, 2017). Additional laboratory measurements on IDDP-2 sample are required to evaluate the effect of pore pressure and fluid-rock interactions on electrical conductivity.

At an effective pressure of about 70-100 MPa (a pressure expected between 3.5 and 4.5km depth when considering a pore pressure of 30-35 MPa), the difference between high frequency velocities on dry samples and low frequency velocities calculated on liquid-saturated samples is significant (about $300 \text{ m}\cdot\text{s}^{-1}$ – figure 7A). In addition, low frequency velocities on samples saturated with a supercritical fluid may have the same properties as the one measured at high frequency in the laboratory, given the high compressibility of supercritical fluids. Thus seismic tomography images could be interpreted in terms of fluid nature (liquid vs supercritical) and crack density, given these laboratory data, as proposed by Adelinet et al. (2011).

From seismic investigations focused on the southern tip of the Reykjanes peninsula, Jousset et al. (2016) have reported P-wave velocity of about 5400-5600 m.s⁻¹ in the depth interval of 3500-4500m. These velocities are similar to the ones obtained at 150 MPa on saturated (both subcritical and supercritical) sample PP2. The corresponding crack density is about 0.3 (figure 7C), which reveal the presence of open microcracks and porosity. However, these velocities are much higher than the ones measured in the in-situ effective pressure interval (70-100 MPa). On one hand, if the sample PP2 is assumed to be representative of in-situ crack density and porosity, then this velocity difference could be explained by the presence of a saturating fluid of a higher bulk modulus than a supercritical fluid, for instance of a mixture of supercritical fluid and liquid or by mineral precipitation that could seal the microcracks. On the other hand, if supercritical fluids are expected to dominate in this depth interval, as suggested by Fridleifsson et al. (2018) and Zierenberg et al. (2020), this difference may be explained by a lower crack density and porosity at in-situ conditions compared to PP2 samples. These differences could be attributed to the drilling processes that damaged the sample (e.g. Peter-Borie et al., 2018). Finally, investigation of the V_p/V_s ratio provides the same conclusions. Seismic surveys over the same area provide an average V_p/V_s ratio of 1.78 (Blanck et al., 2018), while laboratory measurements provide an average of 1.73 from about 50 MPa of effective pressure to the highest pressure (Figure 5B). This difference could be explained either by a higher crack density in the PP2 sample than in-situ conditions or a less compressible fluid than a supercritical fluid at in-situ conditions.

7. CONCLUSION

Petrophysical properties of IDDP-2 samples indicate that drilling operations, which involve high thermal cooling rates and decompression, mostly control the porosity and pore topology. Regarding these properties, core samples are probably not representative of in-situ conditions expected in the vicinity of the borehole. Petrophysical experiments under high pressure and temperature may help to simulate in-situ conditions. Preliminary measurements indicate that electrical conductivity and acoustic properties imaged by large-scale geophysical surveys in the vicinity of the IDDP-2 hole are necessarily explained by the presence of hydrothermal fluids whose nature and properties (composition, pressure, density, compressibility) cannot be determined in the light of this study. Additional experiments on IDDP-2 samples at high temperature and pressure, combined with geophysical data and images, either from surface or downhole, are required to better characterize the fluids at depth, in particular supercritical fluids.

ACKNOWLEDGEMENTS

The IDDP-2 drilling was funded by HS Orka, Statoil (Equinor), Landsvirkjun, Orkuveita Reykjavíkur, and the National Energy Authority in Iceland. The IDDP-2 well has also received funding from the European Union's HORIZON 2020 research and innovation programme under grant agreement No 690771 to DEEPEGS. Funding for obtaining spot cores at Reykjanes and elsewhere was provided by ICDP and the US NSF (grant no. 05076725). The laboratory experiments leading to these results have received funding from the European Community's Seventh Framework Program (FP7) under grant agreement no. 608553 (FP7 Project IMAGE). Christophe Nevado et Doriane Delmas are thanked for the high quality polished thin sections. All these are greatly acknowledged.

REFERENCES

- Adelinet, M., Dorbath, C., Le Ravalec, M., Fortin, J., and Guéguen, Y. : Deriving microstructure and fluid state within the Icelandic crust from the inversion of tomography data, *Geophys. Res. Lett.*, 38, (2011) L03305, doi:10.1029/2010GL046304.
- Bali, E., L.E. Aradi, A. Szabo, R.A. Zierenberg, G.Ó. Friðleifsson, C. Szabo. Fluid inclusions in the deepest part of the IDDP-2 drill core, Reykjanes Peninsula, Iceland. *Proceedings World Geothermal Congress*, (2020).
- Blanck, H., Jousset, P., Hersir, G.P., Ágústsson, K., Flóvenz, O.G. Analysis of 2014–2015 on- and off-shore passive seismic data on the Reykjanes Peninsula, SW Iceland, *Journal of volcanology and geothermal research*, in press, (2018).
- Boudier, F., Nicolas, A. and Mainprice, D., 2005 : Does anisotropy of thermal contraction control hydrothermal circulation at the Moho level below fast spreading oceanic ridges, *International Geology Review*, 47, (2005).
- Brown, J.M., Ross, J.A., Ross, N.L.: elasticity of plagioclase feldspars, *Journal of Geophysical Research*, 121, (2016), 663-675doi:10.1002/2015JB012736.
- Brown, J.M., Abramson, E.H.: Elasticity of calcium and calcium-sodium amphiboles, *Physics of the Earth and planetary interiors*, 261, (2016), 161-171.
- Einaudi, F., Pezard, P., Ildefonse, B., Glover, P., 2005. Electrical properties of slowspreading ridge gabbros from ODP Hole 1105A, SW Indian Ridge. In: Harvey, P.K., Brewer, T.S., Pezard, P.A., Petrov, V.A. (Eds.), *Petrophysical Properties of Crystalline Rocks: Geological Society, London, Special Publications*, 240, pp. 179–193, doi:10.1144/GSL.SP.2005.240.01.14.
- Fortin, J., Guéguen, Y., and Schubnel, A.: Effects of pore collapse and grain crushing on ultrasonic velocities and V_p/V_s , *J. Geophys. Res.*, 112, (2007), doi:10.1029/2005JB004005.
- Fortin, J., Sanchits, S., Vinciguera, S. and Guéguen, Y. :Influence of thermal and mechanical cracks on permeability and elastic wave velocities in a basalt from Mt. Etna volcano subjected to elevated pressure, *Tectonophysics*, 503, (2011), 60-74.
- Fridleifsson, G.Ó., Elders, W.A., Zierenberg, R.A., Fowler, A.P.G., Weisenberger, T., Mesfin, K.G., Sigurdsson, O., Nielsson, S., Einarsson, G., Óskarsson, F., Gudnason, E.A., Tulinius, H., Hokstad, K. , Gibert, B., Nono, F., Loggia, D., Parat, F., Cichy, S.B., Escobedo, D., Mainprice, D. : The Iceland Deep Drilling Project at Reykjanes: Drilling into the root zone of a black smoker analog, *Journal of volcanology and Geotherma lResearch*, (2018), in press.
- Gassmann, F. : Uber die elasticizät poröser medien, *Vierteljahrsachr. Naturforsch. Ges. Zurich*, 96, (1951) 1–23.
- Ghassemi, A., Tarasovs, S., Analysis of Fracture Propagation under Thermal Stress in Geothermal Reservoirs, *Proceedings World Geothermal Congress*, Melbourne, Australia (2015).
- Glover, P.W.J., Vine, F.J.: Beyond KTB-electrical conductivity of the deep continental crust. *Surv. Geophys.* 16, (1995).

- Guéguen, Y., Dienes, J.: Transport properties of rocks from statistics and percolation. *Mathematical Geology* 21, (1989).
- Ildefonse, B., Pezard, P.: Electrical properties of slow-spreading ridge gabbros from ODP Site 735, Southwest Indian Ridge. *Tectonophysics* (2001) 330, 69–92, doi:10.1016/S0040-1951(00)00220-1.
- Jousset, P., Blank, H., Franke, S., Metz, M., Agustsson, K., Verdel, A., Ryberg, T., Hersir, G.P., Weemstra, K., Bruhn, D.: Seismic tomography in Reykjanes, SW Iceland, Proceedings of the European Geothermal Congress (2016).
- Karlsdottir, R., Vilhjalmsón, A.M., Guðnason, E.A.: Three dimensional inversion of magnetotelluric (MT) resistivity data from Reykjanes high temperature field in SW-Iceland, *Journal of Volcanology and geothermal research*, (2018)
- Keshavarz, M., Pellet, F.L., Loret, B.: Damage and changes in mechanical properties of a Gabbro thermally loaded up to 1,000°C, *Pure and applied geophysics* (2010), DOI 10.1007/s00024-010-0130-0
- Kummerow, J., Raab, S., Schuessler, J.A., Meyer, R.: Non-reactive and reactive experiments to determine the electrical conductivities of aqueous geothermal solutions up to supercritical conditions, *Journal of Volcanology and Geothermal Research*, (2018).
- Lévy, L., Gibert, B., Sigmundsson, F., Hersir, G.P., Flóvenz, O., Briole, P., Pezard, P.A.: The role of smectites in the electrical conductivity of active hydrothermal systems: electrical properties of core samples from Krafla volcano, Iceland, *Geophysical Journal International* (2018), 215, 1558–1582.
- Nono F., Gibert, B., Parat, F., Loggia, D., Cichy S.B, Violay, M.: The electrical conductivity of Icelandic deep geothermal reservoirs: insight from laboratory experiments. *Journal of Volcanology and Geothermal Research* (2018), in press.
- Peter-Borie M., Loschetter, A., Blaisonneau, A., Hieu Tran, V., Gaucher, E., Sigurdsson, O., Fridleifsson, G. Ó, Damy, P.C., Le Lous, M., Tulinius, H.: Thermal stimulation of the deep geothermal wells: insights from the H2020- DEEPEGS project, Proceedings of the European Geothermal Congress, Den Haag, the Netherlands (2019).
- Peter-Borie M., Loschetter, A., Merciu, I.A., Kampf, G., Sigurdsson, O.: Borehole damaging under thermo-mechanical loading in the RN-15/IDDP-2 deep well: towards validation of numerical modeling using logging images, *Geothermal Energy* (2018), 6, 17.
- Pezard, P.A., 1990 : Electrical properties of Mid-Ocean Ridge Basalt and implications for the structure of the upper oceanic crust in Hole 504B. *Journal of Geophysical Research* 95, (1990).
- Pezard, P. A., Howard, J.J., Goldberg, D.: Electrical conduction in oceanic gabbros, Hole 735B, Southwest Indian Ridge. In: Von Herzen, R. P., Robinson, P. T. et al. Proceedings of the Ocean Drilling Program, Scientific Results, (1991) 118, 323-331.
- Scott S., Driesner T., and Weis P.: Geological controls on supercritical resources above magmatic intrusions, *Nature*, (2016). DOI: 10.1038/ncomms8837.
- Sinmyo R and Keppler, H.: Electrical conductivity of NaCl-bearing aqueous fluids to 600C and 1 GPa, *Contrib. Mineral Petrol*, 172, (2017).
- Violay, M., Pezard, P.A., Ildefonse, B., Belghoul, A., Laverne, C.: Petrophysical properties of the root zone of sheeted dikes in the ocean crust: A case study from Hole ODP/IODP 1256D, Eastern Equatorial Pacific, *Tectonophysics*, (2010), doi:10.1016/j.tecto.2010.07.013.
- Violay M., Gibert B., Mainprice D. and Burg J.-P.: Brittle versus ductile deformation as the main control of the deep fluid circulation in oceanic crust. *Geophys. Res. Lett.* (2015) 42, 2767–2773.
- Wagner, W, Pruß, A.: The IAPWS Formulation 1995 for the Thermodynamic Properties of Ordinary Water Substance for General and Scientific Use, *Journal of Physical and Chemical Reference Data*, 31, (2002) 387-535.
- Weidner, M.T. and Vaughan, D.J.: Elasticity of pyroxenes: effects of composition versus crystal structure, *Journal of Geophysical research*, 87, (1982).
- Zierenberg, R.A., G.Ó. Friðleifsson, W.A. Elders, P. Schiffman, A.P.L. Fowler, M. Reed. Active Basalt Alteration at Supercritical Conditions in IDDP-2 Drill Core, Reykjanes, Iceland. Proceedings World Geothermal Congress, (2020).